High-temperature structural phase transition in $Ca_2Fe_2O_5$ studied by *in-situ* X-ray diffraction and transmission electron microscopy

Hannes Krüger [a,*], Volker Kahlenberg [a], Václav Petříček [b], Fritz Phillipp [c], Waltraud Wertl [a]

[a] *Institute of Mineralogy and Petrography, University of Innsbruck, Innrain 52, 6020 Innsbruck, Austria*
[b] *Institute of Physics, Academy of Sciences of the Czech Republic, v. v. i., Na Slovance 2, 182 21 Praha, Czech Republic*
[c] *Max Planck Institute for Metals Research, Stuttgart Center for Electron Microscopy, Heisenbergstraße 3, 70569 Stuttgart, Germany*

ABSTRACT

$Ca_2Fe_2O_5$ shows a first-order phase transition from space group *Pnma* to a modulated structure described in superspace group $Imma(00\gamma)s00$. The transition starts at 947 K during heating and the reverse transition in cooling conditions starts at 923 K, as determined from differential thermal analysis. *In-situ* high-temperature single-crystal X-ray diffraction experiments revealed a phase coexistence over a range of ca. 25 K. Data collected in this range show a good fit to a combined model of the two simultaneously occurring phases, which was refined using the software JANA2006. *In-situ* high-temperature transmission electron microscopy (selected area diffraction, dark field and high resolution images) was utilized to prove the existence of *Pnma* and $Imma(00\gamma)s00$ domains within the temperature range of the phase coexistence. Remaining planar defects were observed within the *Pnma* phase at temperatures below the phase transition. From the analysis of high-resolution electron micrographs, these defects were proven to be antiphase boundaries with a displacement vector of $\mathbf{R} = \frac{1}{2}[111]$.

© 2009 Elsevier Inc. All rights reserved.

1. Introduction

Brownmillerite-type compounds ($A_2B_2O_5$ and $A_2BB'O_5$) are among the most frequently studied oxygen-deficient perovskites (for an overview of these materials see [1] and citations therein).

The mineral *brownmillerite* corresponds to the composition Ca_2AlFeO_5, which crystallizes in space group *I2mb* [2]. Brownmillerite represents one composition of the solid solution series $Ca_2(Al_xFe_{1-x})_2O_5$ with $x = 0.5$ [3,4]. The iron end-member $Ca_2Fe_2O_5$ [5,6] (mineral name *srebrodolskite*) adopts space group *Pnma* at ambient conditions ($a = 5.4$, $b = 14.8$, $c = 5.6$ Å). The other end of the solid solution series ($x > 0.7$) is not realized at ambient pressure, but $Ca_2Al_2O_5$ was successfully synthesized using high pressure [7–9].

Many studies on brownmillerite were performed due to the fact that Ca_2AlFeO_5 is one of the four main phases in Portland cement clinkers (see [10,11] and citations). Their magnetic structures and properties have been investigated by many authors [12–17]. Physical properties of $Ca_2Fe_2O_5$, such as electronic and oxygen-ionic transport [18] and catalytic [19] and photocatalytic [20] behavior, have been studied. Usage as catalyst for the combustion of volatile organic compounds [21,22] and for direct

decomposition of NO_x in exhaust streams [23,24] has been examined. Numerous entries in patent databases also highlight a strong interest in brownmillerites for catalytic applications.

Brownmillerite-type structures exhibit two different layers, alternately stacked: (1) perovskite-like sheets of octahedrally coordinated *B* cations and (2) layers of BO_4 tetrahedra, which are corner-linked to form parallel *zweier* single chains. In the $A_2BB'O_5$ brownmillerites *B* and *B'* may adopt the octahedral and tetrahedral sites, respectively. Mixed occupations are observed frequently. For example, in Ca_2AlFeO_5 Al and Fe can be found on tetrahedral and octahedral sites [2–4,25,26], although Al shows a preference for the tetrahedral site.

Two mirror-related configurations of the tetrahedral chains are possible: right-handed (R) and left-handed (L) [27]. The most common space groups for brownmillerites result from these configurations: the centrosymmetric *Pnma* (see Fig. 1a) requires the configuration of the chains to change from one tetrahedral layer to the next tetrahedral layer, whereas the acentric *I2mb* (Fig. 1b) exhibits only one configuration of the chains within the structure.

Structural models in space group *Imma* presuppose statistical disorder of L and R chains. In our view, this is a simplification of superstructures, which arise from an order (periodic or aperiodic) of L and R chains within the tetrahedral layers. Examples of superstructures due to ordering of the chains can be found in [9,28–32]. Generally, the superstructure reflections of such chain

ordering are weak and can easily be missed in powder diffraction patterns.

Two phase transitions are known for the iron end-member $Ca_2Fe_2O_5$: the loss of the antiferromagnetic order at the Néel temperature at ca. 720 K [12,14,33] and a structural phase transition [17,26,33,34] at ca. 950 K. The high-temperature phases of the end-members $Ca_2Fe_2O_5$ and $Ca_2Al_2O_5$ turned out to be isotypic modulated structures [9,31], with an aperiodic sequence of tetrahedral chains. These structures are described using the $(3 + 1)$-dimensional superspace approach [35]. Their superspace group is $Imma(00\gamma)s00$. Our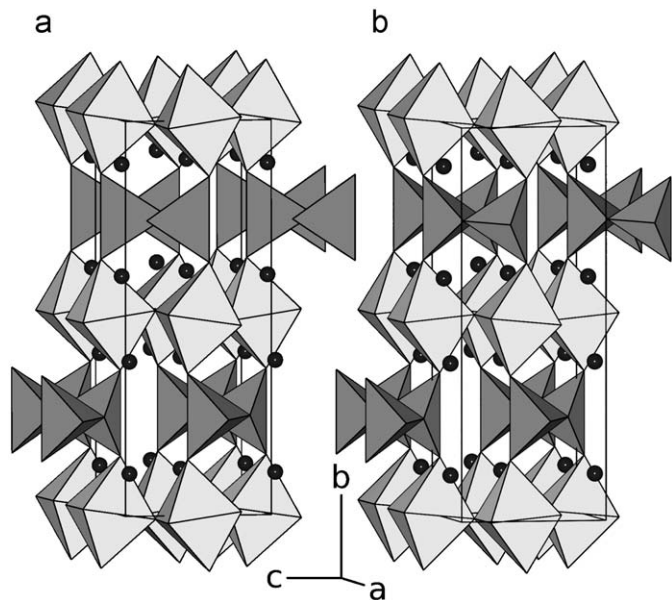 own studies show, that the system $Ca_2(Al_xFe_{1-x})_2O_5$ exhibits modulated HT phases for x up to at least 0.28 [36]. Further details will be reported elsewhere.

2. Synthesis

Single crystals were synthesized using a $CaCl_2$ flux. We used the same sample material as in a former study [31]. More details on the synthesis were given by Kahlenberg and Fischer [37].

Polycrystalline material for the differential thermal analysis (DTA) and transmission electron microscopy (TEM) experiments was synthesized by solid state reactions. Analytical grade (*pro analysi*) $CaCO_3$ and Fe_2O_3 were mixed and ground in an agate mortar, pressed into pellets and heated to 1273 K. In order to achieve a better homogeneity and a more complete reaction, the sample was removed from the furnace after ca. 20 h, pulverized and pressed into pellets again. Subsequently, the heat-treatment was continued for 50 h at 1473 K.

3. Differential thermal analysis

The DTA experiment was performed on a Setaram SetsysEvolution 2400 instrument, using a TGA-DTA1600 transducer, equipped with Pt/Pt-Rh 10% thermocouples. 95.4 mg of the pulverized sample material was filled in a 100 μl Pt crucible. Subsequently, the DTA experiment was carried out with a rate of 5 K/min to a maximum of 1273 K in He atmosphere. The DTA signal of one heating–cooling cycle clearly shows two thermal effects: (1) one weak signal with a maximum at 723 K without hysteresis between heating and cooling, and (2) another weak effect, showing onset temperatures of 947 K (maximum of the peak at 954 K) during heating and 923 K (maximum 915 K) during cooling (Fig. 2). The first signal corresponds to the Néel temperature of the material. Earlier studies of the Néel temperature of $Ca_2Fe_2O_5$ report 703 [33], 716 [38], 720 [14] and 730 K [12]. The second effect is caused by the $Pnma–Imma(00\gamma)s00$ phase transition. The hysteresis of ca. 24 K was not reported in earlier studies. The

Fig. 1. Structures of $Ca_2(Al_xFe_{1-x})_2O_5$ brownmillerites at ambient conditions: (a) space group *Pnma* with alternating layers of R and L-type of tetrahedral chains, (b) space group *I2mb*, showing one type of tetrahedral chains only. Black spheres depict Ca atoms.
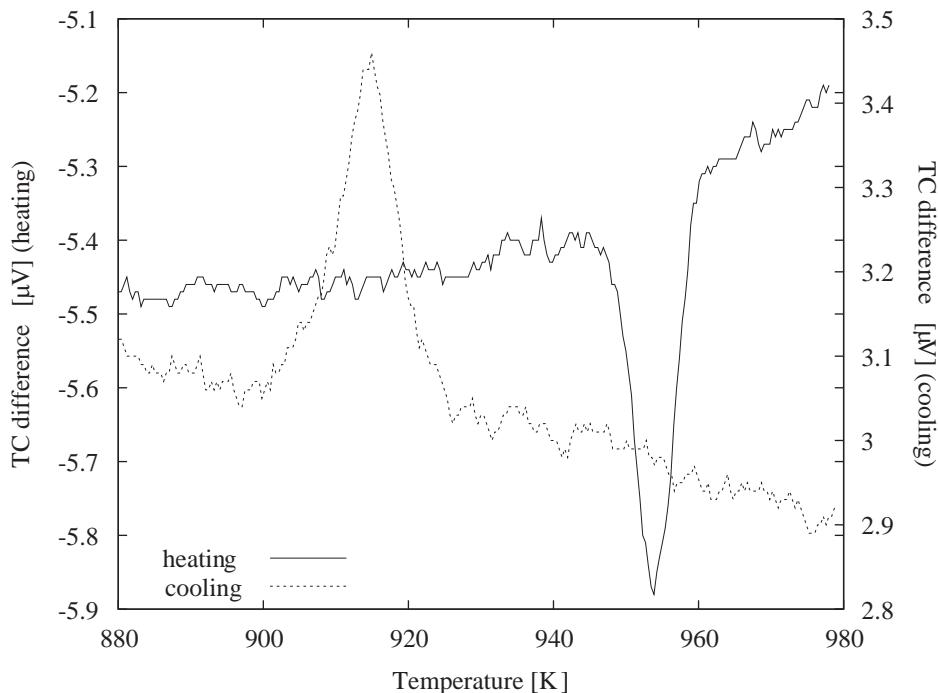

Fig. 2. Differential thermal analysis showing the signals of the $Pnma–Imma(00\gamma)s00$ transition. The hysteresis between the onset temperatures is ca. 24 K.

following values of T_c were given for this transition: 958 [34], 961 [38] and 997 K [26]. Possible reasons for the large spread of these values will be discussed later.

4. High-temperature single-crystal X-ray diffraction (XRD)

4.1. Experimental

Single-crystal X-ray diffraction experiments were carried out with a STOE IPDS-II (two-circle goniometer, image plate detector) diffractometer. For high-temperature data collection a Heatstream device (STOE & Cie GmbH) was used, which provides a hot N_2 gas flow. The heater was operated at a constant flow of 0.8 l/min N_2 (regulated by a mass flow controller).

To calibrate the temperature, a type K thermocouple (STOE & Cie GmbH) at the sample position was used to record the temperature vs the heating current. To account for deviations due to the mounting of the samples, phase transitions of polycrystalline K_2SO_4 and K_2CrO_4 (embedded in SiO_2 glass capillaries, as used for mounting the single crystals) were observed by temperature-dependent measurements of X-ray powder diffraction patterns. The known phase transition temperatures [39,40] were used to correct the previously obtained calibration function. The obtained accuracy is better than ± 5 K.
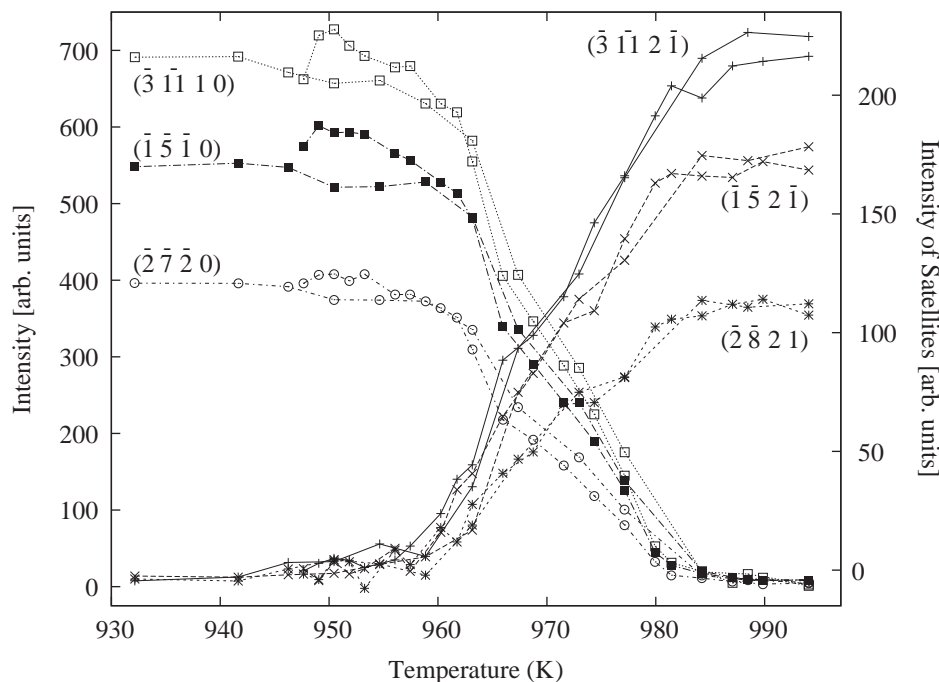

Fig. 3. Temperature dependence of selected reflections: $h + k + l \neq 2n$ main reflections belong to the *Pnma* phase (left intensity scale); satellite reflections belong exclusively to the modulated HT phase (right scale).

Table 1
Details of the refinements.

Temperature (K)	961.8	963.1	966.0	968.8	971.6	974.3	977.2	980.0
Fraction of HT phase	0.083(6)	0.103(7)	0.307(11)	0.411(11)	0.528(11)	0.609(10)	0.714(10)	0.885(5)
Refl. measured (obs/all)	1373/2827	1462/2821	1632/2822	1699/2823	1722/2822	1714/2826	1760/2827	1673/2820
Main refl. measured (obs/all)	1117/1417	1114/1418	1070/1412	1053/1415	1014/1414	982/1415	970/1414	828/1411
Sat. refl. measured (obs/all)	257/1411	348/1403	562/1410	647/1408	708/1408	733/1411	790/1413	846/1409
Unique refl. (obs/all)	702/1198	753/1199	812/1197	844/1201	837/1198	850/1202	863/1199	827/1197
Unique main refl. (obs/all)	531/622	537/626	518/623	513/624	494/623	491/626	475/623	426/621
Unique sat. refl. (obs/all)	171/576	216/573	294/574	332/577	343/575	359/577	388/576	401/576
R_{merge} (obs/all)	3.96/5.23	4.65/5.67	4.66/5.63	4.59/5.53	4.64/5.68	5.07/6.05	4.91/5.88	4.64/5.71
hklm all reflections								
R (obs/all)	4.17/8.90	4.81/8.75	4.12/7.42	4.37/7.40	4.04/7.36	4.31/7.26	4.53/7.57	4.64/8.31
Rw (obs/all)	3.77/4.30	4.28/4.70	3.61/4.05	3.79/4.17	3.89/4.36	3.78/4.14	3.98/4.35	3.95/4.39
hkl0 main reflections								
R (obs/all)	3.03/4.03	3.81/4.87	3.10/4.50	3.27/4.56	2.95/4.65	3.52/5.27	3.67/5.70	3.89/7.12
Rw (obs/all)	3.13/3.24	3.82/3.89	3.06/3.27	3.15/3.29	2.89/3.13	3.37/3.55	3.51/3.72	3.53/3.89
hklm, |m| = 1 satellite reflections								
R (obs/all)	17.52/38.42	13.65/29.56	9.12/18.61	8.70/16.73	7.76/15.30	6.71/12.64	6.80/12.06	6.26/10.80
Rw (obs/all)	19.32/24.21	13.44/17.49	7.98/9.69	7.29/8.60	7.62/8.81	5.36/6.29	5.45/6.23	4.96/5.58

Criterion for observed reflections is $I > 3\sigma(I)$ and weighting scheme based on σ, $w = 1/[\sigma^2(F) + (0.01F)^2]$.

The crystal under investigation (size $0.18 \times 0.18 \times 0.06$ mm) was embedded in a SiO_2 glass capillary. While tracking down the *Pnma* to *Imma*(00γ)*s*00 transition by high-temperature single-crystal XRD experiments, a diffraction pattern was observed, which could not be explained by either one of the known structures. The diffraction pattern exhibits a primitive lattice (indexed with the known orthorhombic brownmillerite unit cell), as well as satellite reflections, which can be indexed with a *q*-vector [35] of $\mathbf{q} = \gamma c^*$. This observation can be explained as a superposition of the diffraction patterns of the low-temperature *Pnma* and the HT *Imma*(00γ)*s*00 phase.

To elucidate the behavior of the phase transition a series of 21 diffraction experiments was performed from 948 up to 994 K in steps of ca. 2 K. Subsequently, 13 experiments were performed from 994 down to 932 K in steps of ca. 5 K. Eight more experiments were carried out in a second heating–cooling cycle between 1016 and 1080 K, to give a more detailed picture of the variation of the modulation wave vector **q**.

All data collections were performed under the same conditions: *K*α radiation from a sealed Mo X-ray tube operated at 50 kV and 40 mA was used. A plane graphite monochromator and a 0.5 mm multiple pinhole collimator were utilized to direct the beam to the sample. The distance between the sample and the detector was set to 100 mm, which corresponds to a maximum diffraction angle of $\theta_{max} = 29.7°$. Measurements were started from the same position of the ω-axis, with 5 min exposure and 1.5° rotation increments of ω per frame. All data collections cover at least a rotation of 15° in ω, most measurements between 958 and 983 K cover ca. 70° (the ones used for the structural refinements).

Fig. 3 shows the individual intensities of six selected reflections (*hklm*) as they change with temperature. To keep the intensities at the same scale, the data was integrated using the same constant scaling factor for all individual data collections [41]. Three of the selected intensities are main reflections ($m = 0$) violating the condition $h + k + l = 2n$, i. e. they are not allowed in the *I*-centered HT phase. Furthermore, three strong satellite reflections ($m \neq 0$) were arbitrarily chosen. First significant intensities of satellite reflections can be observed at ca. 960 K using the described experimental setup and conditions. At the same temperature, the selected $h + k + l \neq 2n$ reflections start to decrease in intensities until they disappear at ca. 985 K. This observation can be interpreted as a 25 K wide range of phase coexistence with varying volume fractions of the two phases.

4.2. Multiphase refinement from single-crystal data

Whereas crystal structure refinements of multiphase systems are routine work in quantitative powder diffractometry (Rietveld analysis), there are only a few examples of multiphase refinements carried out with single-crystal data, although the term single crystal is not valid in a strict sense here.

All known examples [42–46] show systematically intergrown structures with partly coinciding diffraction patterns. To the best of our knowledge, this is the first application of multiphase refinements to a 3-dimensional/(3 + 1)-dimensional incommensurate system using single-crystal data. In this case, the diffraction pattern can be indexed with one basic cell, which stays the same in size (except thermal expansion) and orientation during the transition, even though the lattices differ in centering and *q*-vector. Apart from the 'flipping' of some tetrahedral chains (in order to change their orientation) the structural changes over the phase transition are small and continuous. These properties justify the use of the term *single crystal*, even if the crystal consists of domains with slightly different structures.

The data reduction process included corrections for Lorentz-, polarization- and air-absorption effects, as well as a correction accounting for sample absorption [41]. This was done using eight indexed faces, describing the crystal morphology. The absorption correction was performed under the assumption that the whole crystal volume diffracts consistently. This will only be the case if the domains are distributed randomly within the crystal. The validity of the absorption correction was confirmed by the fact, that the achieved improvement of R_{merge} was very similar (ca. 2%) for all datasets. The redundancy of each data set is 2.3, with a completeness $>97\%$.

Merging of the data did not require special precautions, since both diffracting structures belong to the same point group *mmm*. While applying the reflection conditions all intensities have to be used, which are allowed in either *Pnma* or *Imma*(00γ)*s*00.

Because both structures share the same basic lattice, with perfect overlap of the reflections, the combined intensities are the sum of each phase's contribution. Thus, the combined structure factors can be calculated by

$$F(\mathbf{H}) = \sqrt{\sum_n v_n F_n^2(\mathbf{H})} \tag{1}$$

with v_n giving the relative proportion of phase *n*, their sum $\sum_n v_n$ is normalized to 1. In our case with two diffracting phases, one additional parameter is required in the refinement to account for
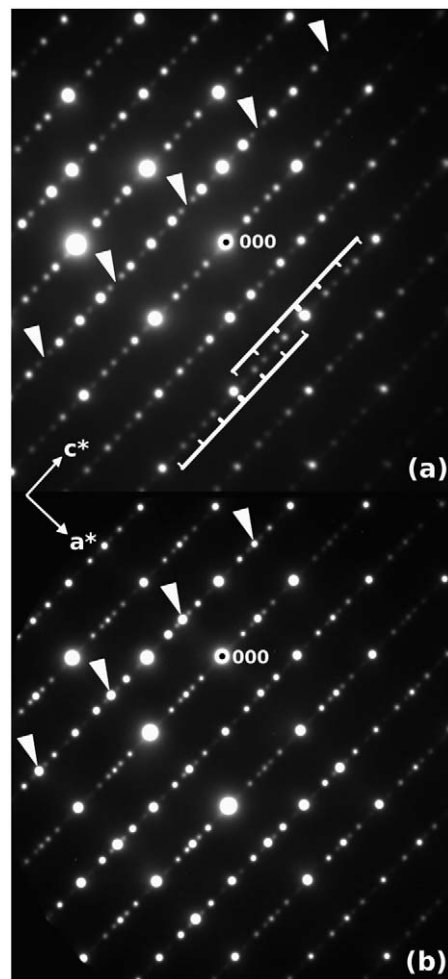

Fig. 4. Electron diffraction patterns (zone axis [010]) of (a) the modulated HT phase at 1100 K (comb-shaped markers indicate main reflections (center) and up to third-order satellites) and (b) the two-phase domain structure at 973 K. Arrowheads mark missing *P*-lattice reflections in (a) and existing ones in (b).
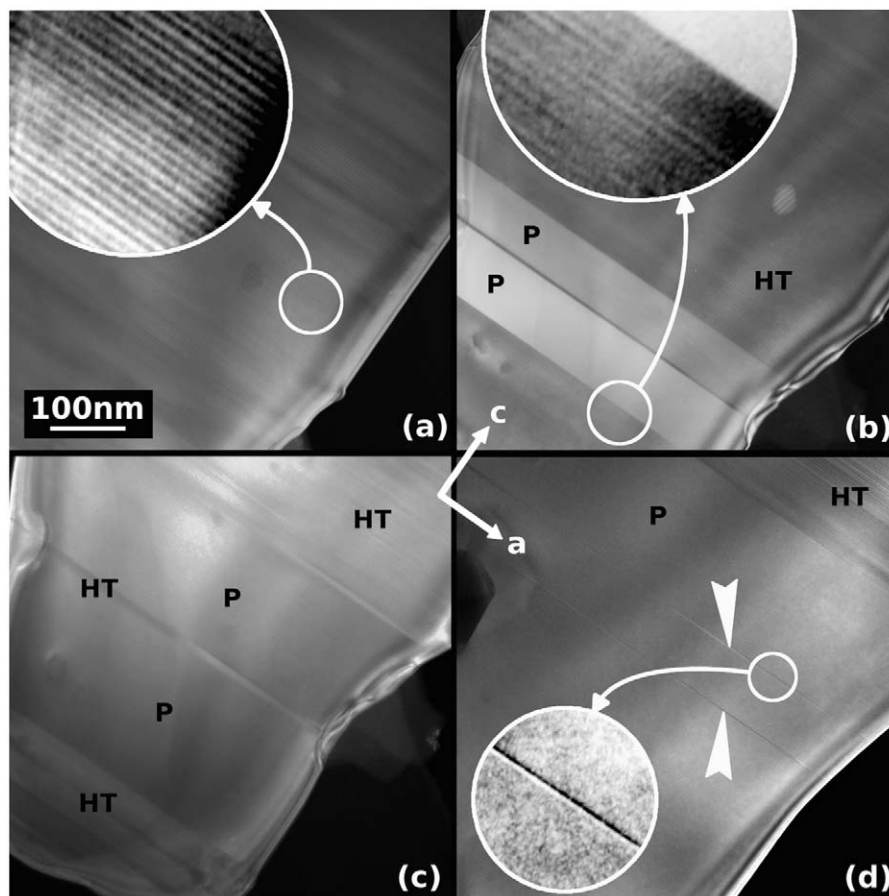
Fig. 5. Dark field TEM images of the domain structure. Domains of the *Pnma* and *Imma*(00γ)s00 are labeled with P and HT, respectively. The temperature was lowered from 995 K (a) to 948 K (d). (a) The whole crystal grain shows the modulated structure. (b) Domains of the *Pnma* phase occurred. (c) Domains of the *Pnma* phase are getting larger. (d) Remaining antiphase boundaries are marked with arrows.
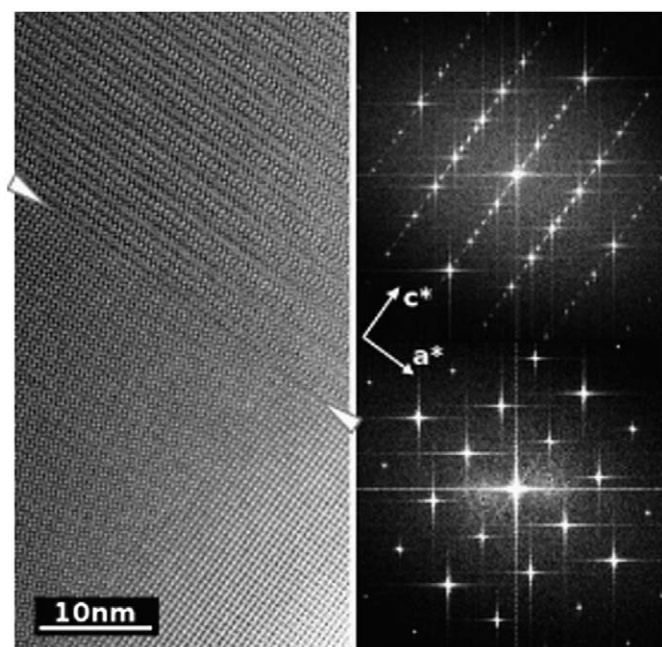

Fig. 6. High-temperature HRTEM (zone axis [010]) of a phase boundary between domains of the *Pnma* (lower left) and *Imma*(00γ)s00 (upper right) structure. Micrograph recorded at 970 K. Corresponding FFT patterns are shown on the right.

the volume ratio of the phases. If the diffraction vector exclusively belongs to one of the phases, the contribution of the other phase to the structure factor is zero. For example, diffraction vectors *hklm* with $m \neq 0$ are caused by the modulated phase only. *hklm* reflections with $m = 0$ and $h + k + l \neq 2n$ are generated by the *P*-lattice low-temperature phase only.

Refinement of multiphase systems from single-crystal data can be performed with Jana2006 [47]. The refinement includes 89 parameters: 45 structural parameters of the low-temperature phase [6] including anisotropic atomic displacement parameters. The superspace-embedded [35] model of the modulated phase contains 42 structural parameters [31]. One scaling factor and the previously mentioned factor to account for the volume ratio of the phases complete the 89. The refinements were performed using structure factors.

The details of eight full-matrix least-squares refinements in the range of 961.8–980 K are given in Table 1. The absolute temperatures are not as precise as given in the table (as discussed above), although the relative accuracy is better than 1 K.

The refinements[1] of the structures show satisfactory *R*-values. The *R*-values of the satellite reflections at 980 K are very similar to those we reported for the modulated phase at 1100 K [31]. At lower temperatures, the satellite *R*-values increase, due to

---

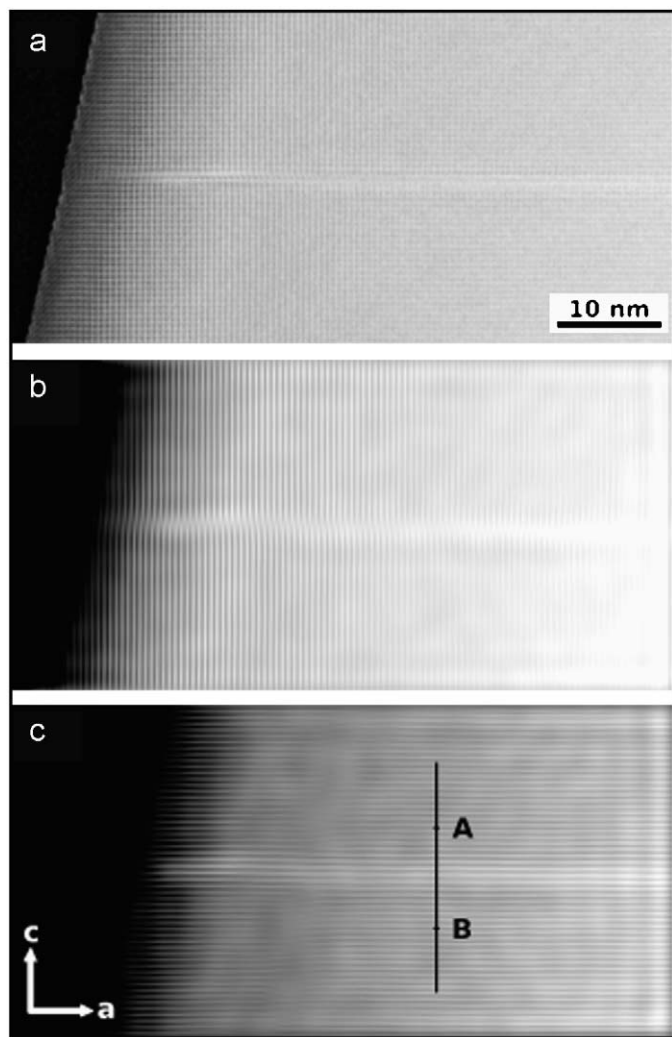[1] The Jana input files needed to reproduce the refinements can be requested from the authors.

Fig. 7. (a) High-resolution electron micrograph of an antiphase boundary. Image taken along the [010] zone axis. The trace of the APB is parallel [100]. (b) and (c) are Fourier filtered using the frequencies parallel and perpendicular to the antiphase boundary, respectively.

was operated at an accelerating voltage of 1.25 MeV, providing a point-resolution of 0.12 nm. The sample was mounted in a double-tilt heating holder (GATAN Model 652-TaM). The accuracy for temperatures given in this section is ±15 K. A drift-compensating device [49] was employed during the acquisition of high-resolution images at elevated temperatures.

Selected area diffraction (SAD) experiments at 1100 K showed the presence of the HT phase by the occurrence of satellite reflections in the electron diffraction (ED) pattern in the (h0l) layer (Fig. 4a). Furthermore, the lattice became I-centered, as expected for the known modulated HT phase. The modulation wave vector was determined to be $\mathbf{q} = 0.58c^*$, which is in good agreement with the XRD results.

By carefully lowering the temperature (to get into the postulated two-phase region), a diffraction pattern showing a primitive lattice, as well as satellite reflections, could be observed and recorded at 973 K (Fig. 4b).

Dark-field images show that domains of the modulated HT-phase are present next to domains of the low-temperature phase, sharing the same basic lattice (Fig. 5a–d). The objective aperture was placed in a way to achieve a diffraction contrast between the phases. Domains of the modulated structure can be identified by periodic fringes caused by the modulation (see enlarged regions in Fig. 5a and b).

High-resolution micrographs were taken of the observed phase boundaries. Fig. 6 shows a Pnma–Imma(00γ)s00 phase boundary at 970 K. The corresponding FFT patterns are calculated using IMAGEJ [50]. The figure shows that the satellite reflections, which can be seen in the FFT pattern, originate only from the upper part of the micrograph.

The width of the domains showed a dependence on the temperature. As the temperature was lowered, the low-temperature phase domains grew (Fig. 5b–d), until no HT-phase domains remained. Some residual defects could be observed at temperatures below the two-phase region (Fig. 5d), which can be attributed to remaining antiphase boundaries (APBs). A high-resolution micrograph (Fig. 7a) of such a defect clearly shows, that it is an antiphase boundary. Fig. 7b and c are derived from Fig. 7a by the Fourier-filtering technique: the Fourier transform of Fig. 7a was computed. Masks were used on the frequency domain image to pass only the frequencies parallel (Fig. 7b) or perpendicular (Fig. 7c) to the inverse Fourier transform to derive the filtered images. This was performed using IMAGEJ [50].

The phase shift parallel to the APB (along [100]) can be easily seen in Fig. 7b. The component along [001] (perpendicular to the APB) is not as easy to identify in Fig. 7c. In order to visualize the phase shift in this direction an intensity profile along [001] crossing the APB is derived from Fig. 7c (along the shown black line). Equidistant vertical lines representing the lattice periodicity are added to the intensity plot in Fig. 8. In the left part of the plot these lines are in sync with the maxima and on the right side they coincide with the minima. The phase shift of $\frac{1}{2}$ along [001] associated with the APB occurs in the center, which can be seen between pixels 190 and 210.

In the Imma(00γ)s00–Pnma transition the centering vector $\frac{1}{2}$[111] is lost. APBs are formed if different (by a displacement vector of $\mathbf{R} = \frac{1}{2}$[111]) domains of the Pnma structure grow and contact together. This could be observed during the TEM experiments. The APBs are oriented parallel to [100]. Whether they are parallel or inclined in respect to [010] cannot be concluded from our experiments, since the observations were made along [010]. The structure of such an APB can be interpreted as follows: the substructure of the octahedral layers stays intact, whereas the configuration of the tetrahedral layers changes across the APB. A possible APB perpendicular to [001] is modeled in Fig. 9.
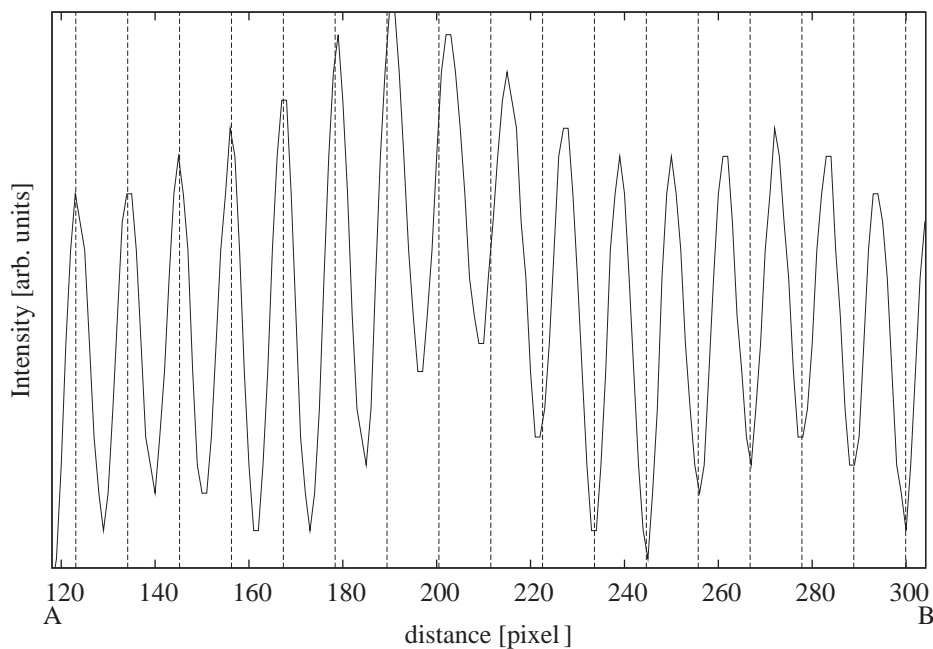
decreasing intensities of the satellite reflections. At 980 K ca. 70% of the measured satellites were considered to be observed [$I > 3\sigma(I)$]. Their average $I/\sigma(I)$ ratio is ca. 13. The satellites of the data set collected at 961.8 K show an average $I/\sigma(I)$ of less than 3, and only 30% of them are observed.

The R-factors for the main reflections show the smallest values for the lower temperatures, slightly increasing with the temperature. This can be understood from the fact that the number of observed main reflections decreases as the low-temperature phase vanishes. Consequently, the best fit to all reflections (main and satellite) is obtained at the phase composition close to 1:1.

5. Transmission electron microscopy

Polycrystalline material of $Ca_2Fe_2O_5$ was further pulverized in an agate mortar, dispersed in ethanol by sonication and subsequently applied to a holey carbon film on a copper grid.

Transmission electron microscopy was performed using the Stuttgart JEOL JEM-ARM1250 high-voltage atomic resolution microscope in its side-entry configuration [48]. The microscope

Fig. 8. Intensity profile along [001] obtained from Fig. 7c along the shown profile between A and B. The periodic vertical lines correspond to the lattice spacing. The antiphase boundary can be detected by the phase shift of $\frac{1}{2}$, which occurs between 190 and 210 pixels.
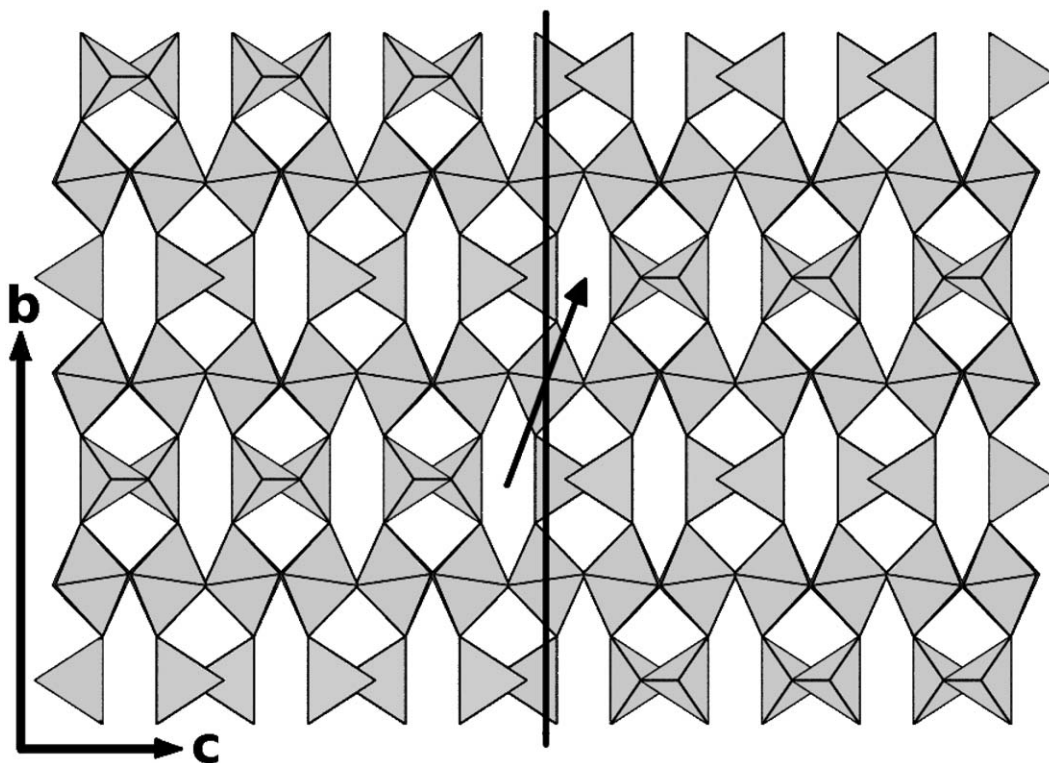

Fig. 9. A model showing an APB perpendicular to [001]. The trace of the displacement vector $\mathbf{R} = \frac{1}{2}[111]$ is shown in black. Ca atoms are omitted.

6. Discussion

The various phase transition temperatures reported in the literature have to be discussed: they range from 958 [34] to 997 K [26]. This large range is not suprising, since we know that both phases coexist over ca. 25 K. Furthermore, the transition temperatures are determined using different techniques, such as powder X-ray or neutron diffraction and DTA. The powder

diffraction based studies monitored the intensity of $h+k+l\neq2n$ reflections to detect the phase transition. This method gives the higher limit (last observability of the *Pnma* phase) of the transition, but is susceptible to the measurement conditions (e.g. strong background) and temperature calibration of the experiment. In DTA studies differences can occur depending on how the phase transition temperature is derived from the thermal signals. Woermann et al. [33] report 963 K. From

Fig. 9 in [33] it can be concluded, that this value corresponds to the peak maximum. The onset temperature is approximately 15 K lower, which is in agreement with our DTA experiments.

The existing literature already shows evidence for the modulated high-temperature phase. In high-temperature powder diffraction patterns of $Ca_2Fe_2O_5$, five unindexed peaks (18.9, 19.8, 20.8, 26.1 and 27.8° 2θ, Cu-radiation) were mentioned by Redhammer et al. [26], which were 'seen as an indication for an incommensurate modulation'. Indeed, the latter four of this set can be indexed as $(110\bar{1})$, $(121\bar{1})$, $(130\bar{1})$ and $(112\bar{1})$ satellite reflections. Fig. 3a in [26] also supports a temperature range of coexisting phases, due to the fact that the (131) reflection can be seen together with two satellites. Berastegui et al. [17] mentioned two unindexed diffraction peaks at 3.4 and 3.2 Å. A closer look at Fig. 4b in [17] reveals at least two more unindexed peaks, namely at ca. 2.95 and 2.3 Å. Comparison with a simulated neutron diffraction pattern (using the model of the modulated structure [31]) shows that these peaks can be indexed as the $(130\bar{1})$, $(112\bar{1})$, $(101\bar{1})$ and $(141\bar{1})$ satellite reflections.

From the presented results it is clear that the $Pnma–Imma(00\gamma)s00$ transition in $Ca_2Fe_2O_5$ is of first order. The hysteresis found in the DTA experiment, and the phase coexistence do not conform with a second-order phase transition as proposed by Berastegui et al. [17]. The tetrahedral chains cannot be 'flipped' from one to the other configuration without discontinuous movement of the anions.

Lattice parameters and thermal expansion of $Ca_2Fe_2O_5$ were studied in several [17,26,34] works by powder diffraction methods. Hence, we refrain from reporting less accurate values from the single-crystal measurements. However, the modulation wave vector $\mathbf{q} = \gamma c^*$ requires further discussion, due to its interesting behavior. Fig. 10 shows γ (the only non-zero component of $\mathbf{q}$) and its evolution with temperature.

The q-vectors were refined from ca. 150 up to ca. 1000 control reflections, utilizing the software X-Area [41].

Even though the values show some scatter, the following conclusions can be made: First satellites appear at 960 K with a γ of approximately 0.607. With raising temperatures, γ increases and reaches a maximum of ca. 0.614 around 985 K. From that point γ decreases down to 0.6 at 1080 K. A value of ca. 0.588 was reported earlier for 1100 K [31], which fits to the extrapolated trend. During cooling the values are significantly smaller (the maximum at ca. 0.614 is less pronounced), which is evidence for a hysteresis of structural features of the modulated phase.

In this context the influence of the modulation wave vector on the type of the superstructure is interesting. The superstructures are characterized by the sequence of R and L tetrahedral chains within the layers. The given superspace-embedded structural model in superspace group $Imma(00\gamma)s00$, with $\gamma = 0.5$ would lead to a superstructure with an alternating and periodic (RL) chain sequence (as e.g. found Sr_2MnGaO_5 [30]). The same model with $\gamma = 1$ is an alternate description of the $Pnma$ structure. Other commensurate superstructures with $\gamma = \frac{2}{3}$ (chain sequence RRL) or $\gamma = \frac{5}{8}$ (chain sequence RLRLLRLL) were discovered in $Ca_2Co_{2-x}Al_xO_5$ ($x \approx 0.75$) [29].

If the number of different-neighbors (RL or LR) is given as a ratio of the overall number of chains, this ratio increases linearly from 0% ($\gamma = 1$) to 100% for $\gamma = 0.5$.

Abakumov et al. [51] proposed competing mechanisms as driving forces for a phase transition in $Ca_2MnGa_{1-x}Al_xO_5$. Basically, dipole–dipole interactions (dipole moments are associated with the tetrahedral chains [52]) should favor the alternate chain sequence, which in turn leads to higher distortions in the octahedral layers. Incommensurability allows any ratio of same- and different-neighbor chains, which could be a way to fine-tune the competing forces. The q-vector at 960 K corresponds to 78.5% of different-neighbors. This value then decreases to 77.2% at the maximum of γ. At higher temperatures it increases to 80% ($\gamma = 0.6$) and 82% at $\gamma = 0.588$. It can be assumed that with increasing temperature the structure develops towards the 100% different-neighbors (alternating chains) superstructure.
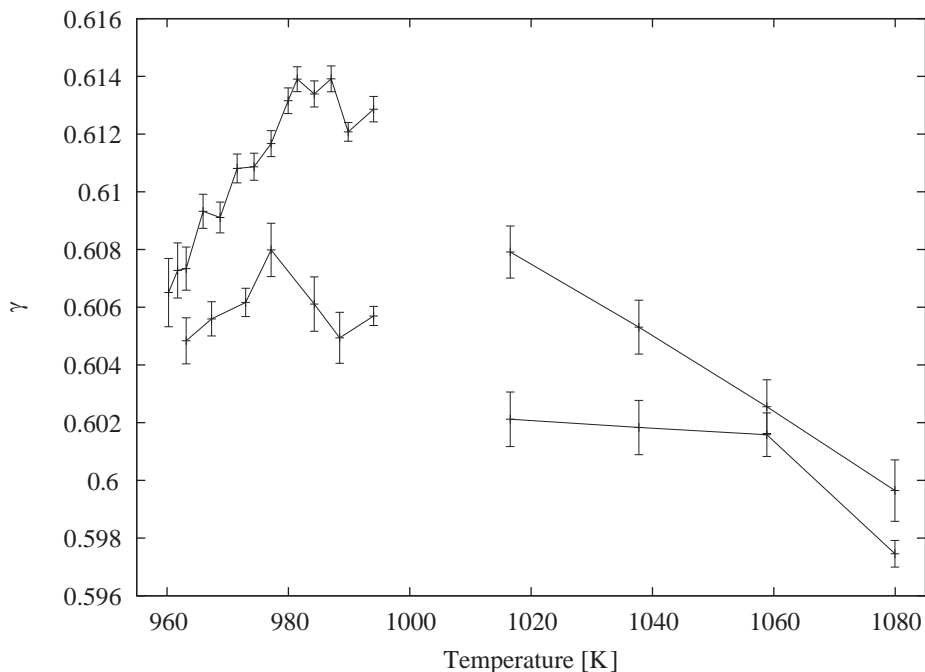

Fig. 10. Temperature dependence of the modulation wave vector $\mathbf{q} = \gamma c^*$. The parameter γ is plotted vs temperature. The two segments at the left are determined from data collections in one heating–cooling cycle. The segments on the right are obtained from a second heating–cooling cycle. Upper plots correspond to heating, lower ones to cooling.

So far, APBs observed in *Pnma* brownmillerites have been reported to be perpendicular to [010] [51,53,54]. Such APBs ($\perp b^*$) produce thin slabs of the *I2mb* structure within the *Pnma* matrix. A compositionally induced phase transition from *Pnma* to *I2mb* is described for $Ca_2MnGa_{1-x}Al_xO_5$. An increasing concentration of APBs is reported, until the displacement vector becomes a new lattice translation [51]. Furthermore, blocks of a superstructure ($\mathbf{q} = \frac{1}{9}b^*$) caused by an ordered sequence of APBs were found in $Ca_2MnGaO_{5.045}$ [53]. However, the APBs we found are not perpendicular to [010], but at least inclined (if not parallel) in respect to [010]. The reasons for the different orientations of the APBs have to be attributed to the formation conditions. In $Ca_2Fe_2O_5$, the orientation of APBs results from the propagation of domain walls during the symmetry reduction from $Imma(00\gamma)s00$ to *Pnma*. The propagation vector of the domain walls clearly is within the *bc*-plane. The existence of a component in *b* cannot be excluded or confirmed without further experiments.

7. Conclusions

The phase transition of $Ca_2Fe_2O_5$ has been studied using two methods complementing one another. HT transmission electron microscopy (ED and high-resolution), as well as HT single-crystal XRD. Both methods derive substantial information, which cannot be obtained from the other. In this case XRD delivers structural information on the atomic level, TEM provides images on a larger scale: distribution of domains and defects. Utilizing multiphase refinements a quantitative measure for the phase composition can be extracted, which—from TEM—is available qualitatively, only. One of the goals of this paper is, to show that multiphase refinements from single-crystal data can provide useful information in phase transition studies with coexisting phases. The software JANA2006 is able to handle multiphase refinements even in cases where modulated structures are involved.

Acknowledgments

References

[1] E.V. Antipov, A.M. Abakumov, S.Y. Istomin, Inorg. Chem. 47 (19) (2008) 8543–8552.
[2] A.A. Colville, S. Geller, Acta Crystallogr. B 27 (12) (1971) 2311–2315.
[3] D.K. Smith, Acta Crystallogr. 15 (11) (1962) 1146–1152.
[4] F. Pobell, F. Wittmann, Phys. Lett. 19 (3) (1965) 175–176.
[5] E.F. Bertaut, P. Blum, A. Sagnières, Acta Crystallogr. 12 (2) (1959) 149–159.
[6] J. Berggren, Acta Chem. Scand. 25 (10) (1971) 3616–3624.
[7] P.S. Aggarwal, J.A. Gard, F.P. Glasser, G.M. Biggar, Cem. Concr. Res. 2 (3) (1972) 291–297.
[8] V. Kahlenberg, R.X. Fischer, C.S.J. Shaw, Am. Mineral. 85 (7–8) (2000) 1061–1065.
[9] B. Lazić, H. Krüger, V. Kahlenberg, J. Konzett, R. Kaindl, Acta Crystallogr. B 64 (4) (2008) 417–425.
[10] A.J. Majumdar, Trans. Br. Ceram. Soc. 64 (1965) 105–119.
[11] H.F.W. Taylor, Cement Chemistry, second ed., Thomas Telford, London, 1997.
[12] L.M. Corliss, J.M. Hastings, W. Kunnmann, E. Banks, Acta Crystallogr. 21 (1966) A95.
[13] R.W. Grant, S. Geller, H. Wiedersich, U. Gonser, L.D. Fullmer, J. Appl. Phys. 39 (2) (1968) 1122–1123.
[14] T. Takeda, Y. Yamaguchi, S. Tomiyoshi, M. Fukase, M. Sugimoto, H. Watanabe, J. Phys. Soc. Jpn. 24 (3) (1968) 446–452.
[15] S. Geller, R.W. Grant, L.D. Fullmer, J. Phys. Chem. Solids 31 (4) (1970) 793–803.
[16] S. Geller, R.W. Grant, U. Gonser, Prog. Solid State Chem. 5 (1971) 1–26.
[17] P. Berastegui, S.-G. Eriksson, S. Hull, Mater. Res. Bull. 34 (2) (1999) 303–314.
[18] A.L. Shaula, Y.V. Pivak, J.C. Waerenborgh, P. Gaczyński, A.A. Yaremchenko, V.V. Kharton, Solid State Ionics 177 (33–34) (2006) 2923–2930.
[19] L.A. Isupova, S.V. Tsybulya, G.N. Kryukova, A.A. Budneva, E.A. Paukshtis, G.S. Litvak, V.P. Ivanov, V.N. Kolomiichuk, Y.T. Pavlyukhin, V.A. Sadykov, Kinet. Catal. 43 (1) (2002) 122–128.
[20] Y. Yang, Z. Cao, Y. Jiang, L. Liu, Y. Sun, Mater. Sci. Eng. B 132 (3) (2006) 311–314.
[21] D. Hirabayashi, T. Yoshikawa, K. Mochizuki, K. Suzuki, Y. Sakai, Catal. Lett. 110 (3-4) (2006) 269–274.
[22] D. Hirabayashi, Y. Kawamoto, K. Suzuki, J. Soc. Inorg. Mater. Jpn. 14 (327) (2007) 83–91.
[23] S. Shin, Y. Hatakeyama, K. Ogawa, K. Shimomura, Mater. Res. Bull. 14 (1) (1979) 133–136.
[24] J.H. White, A.F. Sammells, J.D. Wander, Catalysts for direct decomposition of NO_x in exhausts, in: Proceedings of the 93rd Air and Waste Management Association's Annual Conference and Exhibition, Salt Lake City, UT, United States, 2000.
[25] A.A. Colville, S. Geller, Acta Crystallogr. B 28 (11) (1972) 3196–3200.
[26] G.J. Redhammer, G. Tippelt, G. Roth, G. Amthauer, Am. Mineral. 89 (2004) 405–420.
[27] T. Krekels, O. Milat, G. Van Tendeloo, S. Amelinckx, T.G.N. Babu, A.J. Wright, C. Greaves, J. Solid State Chem. 105 (2) (1993) 313–335.
[28] A.M. Abakumov, M.G. Rozova, B.P. Pavlyuk, M.V. Lobanov, E.V. Antipov, O.I. Lebedev, G. Van Tendeloo, O.L. Ignatchik, E.A. Ovtchenkov, Y.A. Koksharov, A.N. Vasil'ev, J. Solid State Chem. 160 (2001) 353–361.
[29] S. Lambert, H. Leligny, D. Grebille, D. Pelloquin, B. Raveau, Chem. Mater. 14 (2002) 1818–1826.
[30] A.M. Abakumov, A.M. Alekseeva, M.G. Rozova, E.V. Antipov, O.I. Lebedev, G. Van Tendeloo, J. Solid State Chem. 174 (2003) 319–328.
[31] H. Krüger, V. Kahlenberg, Acta Crystallogr. B 61 (6) (2005) 656–662.
[32] H. D'Hondt, A.M. Abakumov, J. Hadermann, A.S. Kalyuzhnaya, M.G. Rozova, E.V. Antipov, G. Van Tendeloo, Chem. Mater. 20 (22) (2008) 7188–7194.
[33] E. Woermann, W. Eysel, T. Hahn, Polymorphism and solid solution of the ferrite phase, in: Proceedings of the Fifth International Symposium on the Chemistry of Cement, Tokyo, supplementary Paper I-54, 1968, pp. 54–60.
[34] K. Fukuda, H. Ando, J. Am. Ceram. Soc. 85 (5) (2002) 1300–1303.
[35] T. Janssen, A. Janner, A. Looijenga-Vos, P.M. de Wolff, Mathematical, physical and chemical tables, Incommensurate and commensurate modulated structures, in: International Tables for Crystallography, third ed., Kluwer Academic Publishers, Dordrecht, vol. C, 2004 (Chapter 9.8).
[36] H. Krüger, B. Lazić, F. Phillipp, V. Petříček, J. Konzett, V. Kahlenberg, Acta Crystallogr. A 64 (2008) C497–498.
[37] V. Kahlenberg, R.X. Fischer, Eur. J. Mineral. 12 (1) (2000) 129–135.
[38] V. Kahlenberg, R.X. Fischer, C. Weidenthaler, T. Zeiske, High temperature investigations on $Ca_2Fe_2O_5$ using X-ray and neutron diffraction, in: Abstracts of the 17th General Meeting of the International Mineralogical Association, Toronto, Canada, 1998, p. A55.
[39] K.-H. Breuer, W. Eysel, Thermochim. Acta 57 (1982) 317–329.
[40] E.L. Charsley, P.G. Laye, M. Richardson, Thermochim. Acta 216 (1–2) (1993) 331–334.
[41] STOE & Cie GmbH, X-AREA, Darmstadt, Germany, 2005.
[42] K. Friese, O. Jarchow, K. Kato, Z. Kristallogr. 212 (9) (1997) 648–655.
[43] K. Friese, O. Jarchow, K. Kato, Y. Kanke, Z. Kristallogr. 212 (12) (1997) 859–863.
[44] T. Balić-Žunić, E. Makovicky, V. Petříček, D. Topa, Acta Crystallogr. A 58 (2002) C32.
[45] K. Friese, A. Honnerscheiä, M. Jansen, Z. Kristallogr. 218 (2003) 536–541.
[46] L. Bindi, V. Petříček, R.L. Withers, M. Zoppi, P. Bonazzi, J. Solid State Chem. 179 (3) (2006) 729–738.
[47] V. Petříček, M. Dušek, L. Palatinus, JANA 2006, The crystallographic computing system, Institute of Physics, Prague, Czech Republic, 2006.
[48] F. Phillipp, R. Höschen, M. Osaki, G. Möbus, M. Rühle, Ultramicroscopy 56 (1994) 1–10.
[49] R. Höschen, W. Sigle, F. Phillipp, A drift compensating system for electron microscopes, in: Electron Microscopy 1996, Proceedings of the 11th European Conference on Electron Microscopy, The Committee of European Societies of Microscopy, Dublin, vol. 1, 1996, pp. 373–374.
[50] M.D. Abràmoff, P.J. Magalhães, S.J. Ram, Biophotonics Int. 11 (7) (2004) 36–42.
[51] A.M. Abakumov, A.S. Kalyuzhnaya, M.G. Rozova, E.V. Antipov, J. Hadermann, G. Van Tendeloo, Solid State Sci. 7 (7) (2005) 801–811.
[52] O. Milat, T. Krekels, G. Van Tendeloo, S. Amelinckx, J. Phys. I 3 (1993) 1219–1234.
[53] A.M. Abakumov, M.G. Rozova, B.P. Pavlyuk, M.V. Lobanov, E.V. Antipov, O.I. Lebedev, G. Van Tendeloo, D.V. Sheptyakov, A.M. Balagurov, F. Bourée, J. Solid State Chem. 158 (2001) 100–111.
[54] S.Y. Istomin, S.V. Abdyusheva, G. Svensson, E.V. Antipov, Synthesis, J. Solid State Chem. 177 (11) (2004) 4251–4257.